

# Flux evolution and kinematics of superluminal components in blazar 3C345

S.J. Qian<sup>1</sup>

National Astronomical Observatories, Chinese Academy of Sciences, Beijing 100012, China

Compiled by using A&A latex

## ABSTRACT

**Context.** The precessing jet-nozzle scenario previously proposed was applied to model-fit the kinematics of five superluminal components (C19, C20, C21, B5 and B7) of jet-B in blazar 3C345.

**Aims.** Based on a specific pattern for the precessing common trajectory of jet-B, the kinematic properties (including trajectory, coordinates, core separation and apparent velocity) were model-fitted and their flux evolution could be studied.

**Methods.** Through model-simulation of their kinematic behavior, the bulk Lorentz factor, viewing angle and Doppler factor were derived as continuous functions of time and the association of their flux evolution with their Doppler-boosting effect was investigated.

**Results.** The 43GHz light-curves of the five superluminal components can be well interpreted in terms of their Doppler effect. The close association of their flux evolution with the Doppler-boosting effect firmly validate our precessing nozzle scenario and support the traditional point-view that superluminal components are physical entities (traveling shocks or plasmoids) participating relativistic motion toward us at small viewing angles.

**Conclusions.** The model-simulation of kinematic behavior of superluminal components by using our precessing nozzle scenario with specific patterns (helical or ballistic) assumed for the precessing common trajectories yields the model-derived bulk Lorentz factor, apparent speed, viewing angle and Doppler factor as continuous functions of time, which are most applicable to study the connection of flux evolution with Doppler boosting effect for the superluminal components.

**Key words.** galaxies: active – galaxies: jets – galaxies: nucleus – galaxies: individual 3C345

## 1. Introduction

3C345 ( $z=0.595$ ) is a prototypical quasar which has been detected in all wavebands of the entire electromagnetic spectrum from radio/mm, infrared/optical/UV and X-rays to high-energy  $\gamma$  rays (Biretta et al. 1986, Babadzhanyants et al. 1995, Schramm et al. 1993, Moore & Stockman 1984, Wang et al. 2004, Malina et al. 1994, Lobanov & Zensus 1999, Schinzel et al. 2011b, Zensus 1997, Ros et al. 2000). It exhibits remarkable and violent multi-waveband variations and its spectral energy distribution has been extensively monitored and studied, yielding significant results on the physical properties of the source. Studies of the correlation between the variabilities at multi-frequencies (from radio to  $\gamma$  rays) play an important role.

3C345 is one of the firstly discovered quasar having a relativistic jet. VLBI-observations have revealed its parsec structure and monitored the kinematic behavior of superluminal components ejected from the radio core (Qian et al. 1991a, 1991b, 1996, 2009, Klare 2003, Klare et al. 2005, Steffen et al. 1995, Ros et al. 2000, Schinzel et al. 2010a, Lobanov & Roland 2005, Lobanov & Zensus 1994, Zensus et al. 1995, Hardee 1987). The flaring activities of the source at multi-frequencies (from radio to  $\gamma$ -rays) are closely connected with the ejection of superluminal components (e.g., Schinzel 2010b).

VLBI-monitoring observations have also shown that the swing of the knot's ejection position angle could be periodic and caused by its jet-precession. We have tried to in-

terpret the VLBI-kinematics of superluminal components in 3C345 in terms of a precessing jet-nozzle scenario since early years (Qian et al. 1991a, 1991b, 1996, 2009). Recently, Qian (2022a) has tried to make model simulations of the kinematic behavior for twenty-seven superluminal components (measured during a 38yr period) in detail. It was found that these superluminal knots could be hypothetically separated into two groups, which were ejected from a precessing double nozzle (jet-A and jet-B), respectively. Based on this division a precession period of  $\sim 7.3$ yr was derived for both the jet-nozzles.

In a recent paper (Qian 2022b), the flux evolution of five superluminal components (C4, C5, C9, C10 and C22) belonging to jet-A was well explained in terms of their Doppler boosting effect combined with the intrinsic flux variations of the components.

In this paper we present the results of modelfits to the flux evolution for five superluminal components (C19, C20, C21, B5 and B7) belonging to jet-B. Before doing so, we firstly give a brief description of the results obtained in the previous work for the five components belonging to jet-A (Qian 2022b), taking knot C9 as a representative example.

- Based on an assumed helical pattern of precessing common trajectory for jet-A the trajectory distribution of the superluminal components of jet-A is shown in Figure 1 (left panel) for different knots ejected at different precession phases. It clearly demonstrates both the swing of

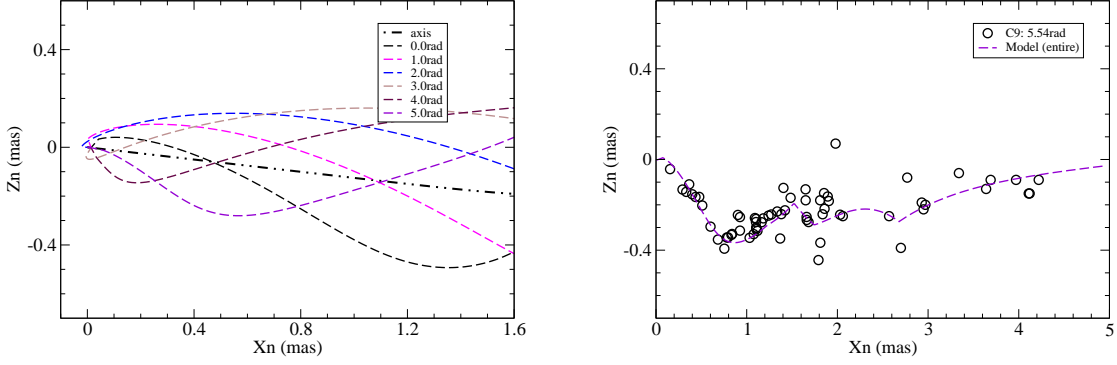


**Fig. 1.** Left panel: Distribution of the precessing trajectories of the superluminal components of jet-A at precession phases  $\phi_0=0.0, 1.0, 2.0, 3.0, 4.0$  and  $5.0$  rad. The jet axis is at position angle of  $-97.2^\circ$ . Jet-A consists of 13 superluminal components (C4 to C14, C22 and C23). The prominent curvatures of the trajectories are caused by the helical pattern assumed for the precessing common trajectory. This distribution demonstrates both the swing of the ejection position angles of the components and different curved tracks for different knots ejected at different precession phases (or ejection times). Right panel: A model-fit to the entire trajectory of knot C9 (ejection time  $t_0=1995.06$  and precession phase  $\phi_0=5.54+2\pi$ ), extending to  $X_n \simeq 4.16$  mas, equivalent to a traveled distance  $Z=106.0$  mas=705 pc. Within  $X_n=1.22$  mas ( $r_n=1.25$  mas or before 1999.94) knot C9 moved along the precessing common trajectory, equivalent to its traveled distance  $Z=44.8$  mas=298 pc.

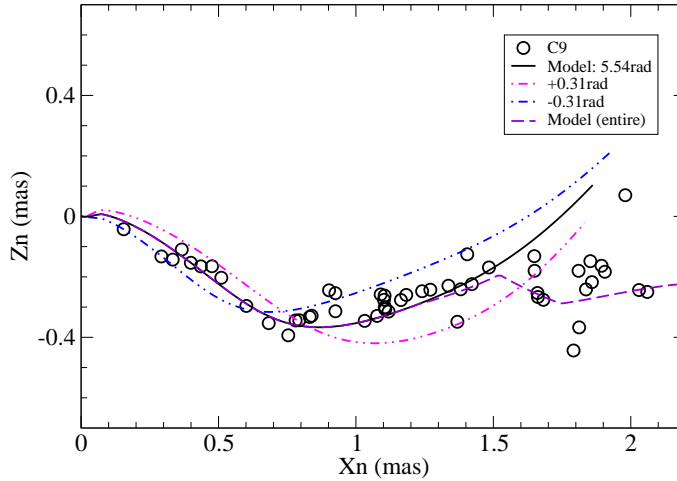


**Fig. 2.** Knot C9: Its inner-jet trajectory ( $X_n \leq 1.5$  mas) exhibits a prominent curvature induced by the helical pattern assumed for the precessing common trajectory. Moreover, most of the data-points are very well fitted into an area delimited by the lines in magenta and blue which are trajectories calculated for precession phase  $\phi_0=5.54 \pm 0.31$  rad, demonstrating that its precession phase was determined with an uncertainty  $\pm 5\%$  of the precession period.

their ejection position angles and different curved tracks coresponding to different ejection times, which have been successfully applied to modelfit the observed kinematics of the superluminal components of jet-A (Qian 2022a, 2022b).

- Generally, the superluminal knots moved along their precessing common trajectories in the inner-jet regions, while they moved along their own individual tracks in the outer jet regions. This transition of trajectory pattern occurred at different core distances for different

knots. The apparent trajectory of knot C9 was measured extending to core distance of  $\sim 4.16$  mas, equivalent to a traveled distance  $Z \sim 106$  mas=705 pc. Its entire trajectory is well fitted in terms of our precessing nozzle scenario as shown in Figure 1 (right). Particularly, its inner trajectory can be very well fitted by the precessing common trajectory pattern (Figure 2), corresponding to a precession phase  $\phi_0=5.54+2\pi$  (or ejection time 1995.06) and extending to a core distance  $\sim 1.25$  mas, which is equivalent to a traveled distance  $Z \sim 44.8$  mas=298 pc.

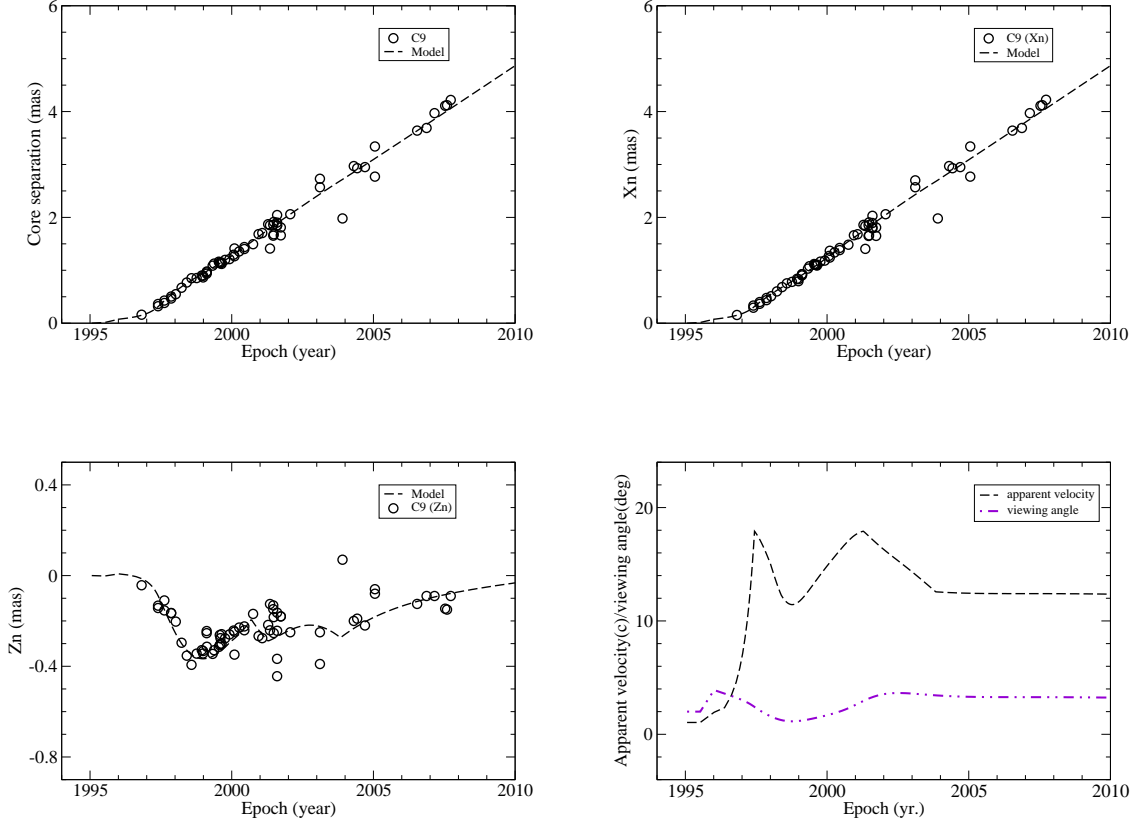


**Fig. 3.** Knot C9: Model fitting of the core separation  $r_n(t)$ , coordinates  $X_n(t)$  and  $Z_n(t)$  (upper two and bottom left panels), and the model-derived apparent speed  $\beta_{app}(t)$  and viewing angle  $\theta(t)$  (bottom right panel) as continuous functions of time.  $r_n$ ,  $X_n$  and  $Z_n$  are very well fitted, especially the fit to the coordinate  $Z_n(t)$ . The model-derived apparent speed  $\beta_{app}$  has an oscillating structure, showing a distinctive pattern of motion: acceleration–deceleration–reacceleration–deceleration. The apparent speed has two maxima at 1997.44 and 2001.28: both  $\beta_{app,max}=17.91$  and the corresponding viewing angles  $\theta=2.41^\circ$  and  $2.94^\circ$ , respectively. The apparent speed has a minimum  $\beta_{app,min}=11.44$  at 1998.77, with a minimal viewing angle  $\theta_{min}=1.14^\circ$ , corresponding to the maximal Doppler factor  $\delta_{max}=31.86$ .

The precessing common trajectory pattern assumed in the scenario for jet-A is also applicable to interpret the trajectories measured for other superluminal knots in jet-A (e.g. C4, C5, C7, C10–C13, C22 and C23; Qian 2022a, 2022b).

- The curved jet-axis and the helical pattern assumed for the precessing common trajectory of jet-A in our scenario result in prominent curvatures in the apparent trajectories of superluminal components (Fig.1, left panel). The remarkable trajectory curvature measured for knot C9 is very well model-fitted in our precessing nozzle scenario (Figure 2). Within  $X_n=1.22$  mas knot C9 moved along the precessing common track. Most of the observed data-points are located extremely well within the area delimited by the red and blue lines which indicate the trajectories calculated for the precession phases  $\phi_0=5.54\pm 0.31$  rad (or  $\pm 5\%$  of the precession period). This distinctively demonstrates that the helical pattern assumed for the precessing common trajectory is appropriate and valid to describe the kinematic behavior of knot C9 and other knots (e.g., C4, C5 and C22; for knot C4, its common track extends to  $X_n\sim 1.14$  mas, equivalent to a traveled distance of  $\sim 267$  pc). Moreover, the

model-fits to the apparent trajectories of multi-knots imply the existence of both a precessing nozzle and a precessing common track of helical pattern.

- For knot C9, its core distance  $r_n(t)$ , coordinates  $X_n(t)$  and  $Z_n(t)$  are well fitted and shown in Figure 3 (upper two and bottom left panels). Both the model-derived apparent velocity  $\beta_{app}(t)$  and viewing angle  $\theta(t)$  as continuous functions of time shown in Figure 3 (bottom right panel) reveal prominent structural details. During the period of  $\sim 1997$ –2005  $\beta_{app}(t)$  exhibits a structure of acceleration/deceleration/reacceleration/deceleration: (a) at 1997.44 (core separation  $r_n=0.33$  mas)  $\beta_{app}=17.91$  (a maximum) and  $\theta=2.41^\circ$ ; (b) at 1998.77 ( $r_n=0.88$  mas)  $\beta_{app}=11.44$  (a minimum) and  $\theta=1.14^\circ$  (a minimum, corresponding to the maximal Doppler factor  $\delta_{max}=31.86$ , see Figure 4 below); (c) at 2001.28 ( $r_n=1.77$  mas)  $\beta_{app}=17.91$  (a maximum) and  $\theta=2.94^\circ$ .
- The bulk Lorentz factor  $\Gamma(t)$  and Doppler factor  $\delta(t)$  derived for knot C9 are shown in Figure 4. During the period of  $\sim 1997.5$ –2001.4 the bulk Lorentz factor  $\Gamma\approx 18.5$ –18.0, while the Doppler factor  $\delta$  has a smooth bump structure, which was completely caused by the change

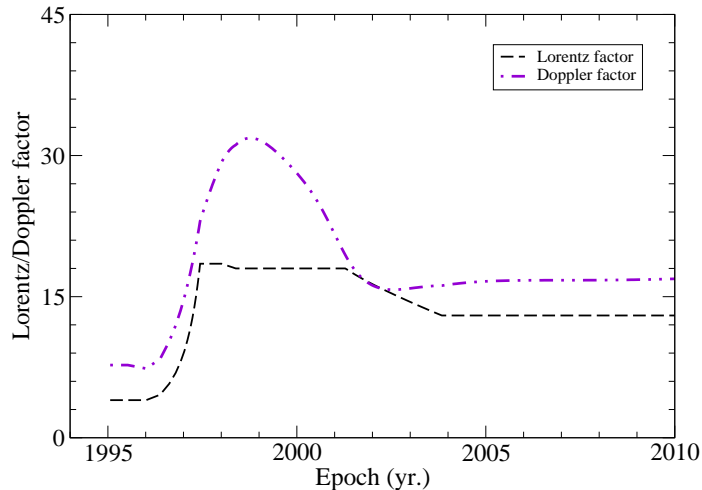


**Fig. 4.** Knot C9: Model-derived bulk Lorentz factor  $\Gamma(t)$  and Doppler factor  $\delta(t)$  as continuous functions of time.  $\Gamma(t)$  has a plateau structure ( $\Gamma \sim 18.5$ – $18.0$ ) during  $\sim 1997.5$ – $2001.5$ , while  $\delta(t)$  has a bump structure with a peak  $\delta_{max} = 31.86$  at 1998.77, when  $\Gamma = 18.00$  and  $\theta = 1.14^\circ$  (a minimum). It is worth noting that the bump structure of Doppler factor is derived completely from the model-fitting of its kinematics only, thus the Doppler boosting effect ( $[\delta(t)/\delta_{max}]^{3+\alpha}$ ) for knot C9 was independently derived or predicted with respect to its flux evolution.

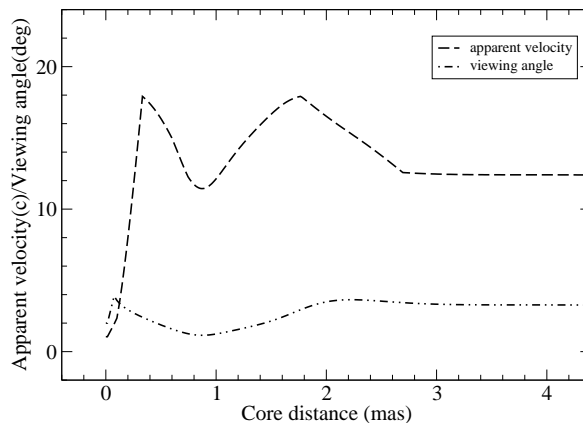


**Fig. 5.** Knot C9: Model-derived apparent speed  $\beta_{app}(t)$  and viewing angle  $\theta(t)$  as functions of core separation  $r_n$ . The two maxima in  $\beta_{app}(t)$  are at  $r_n = 0.33$  mas and  $r_n = 1.77$  mas. Its minimum is at  $r_n = 0.88$  mas. The pattern of motion of knot C9 has a remarkable oscillating structure: acceleration–deceleration–reacceleration–deceleration, which is fully consistent with the results analysed by Jorstad et al. (2005).

in the viewing angle, as shown in Figure 3 (bottom right panel). The maximal Doppler factor is 31.86 at 1998.77 (at  $r_n = 0.88$  mas), coincident with the minimal viewing angle  $\theta = 1.14^\circ$  and minimal apparent speed  $\beta_{app} = 11.44$ .

- In order to compare our results with those obtained by Jorstad et al. (2005) we show the apparent speed  $\beta_{app}$  as a function of core distance  $r_n$  for knot C9 in Figure 5. It exhibits a pronounced oscillating structure with two maxima (both  $\beta_{app,max} = 17.91$ ) at core distances  $r_n = 0.33$  mas and 1.77 mas, and a minimum  $\beta_{app,min} = 11.4$  at  $r_n = 0.88$  mas, corresponding to a minimal viewing angle  $\theta_{min} = 1.14^\circ$ . In addition, the

decreasing part (in the range of  $r_n \sim 1.2$ – $1.8$  mas) of the 43 GHz light curve measured by Jorstad et al. (2005) for knot C9 can be well fitted by the Doppler boosting profile  $S_{int}[\delta(t)/\delta_{max}]^{3+\alpha}$  derived as a function of core distance in this paper as shown in Figure 6. Thus, we unexpectedly find that the model-simulated results obtained within the framework of our precessing nozzle scenario are fully consistent with the phenomena observed and analyzed by Jorstad et al. (2005) as follows:

**The change in apparent speed and the twisted**

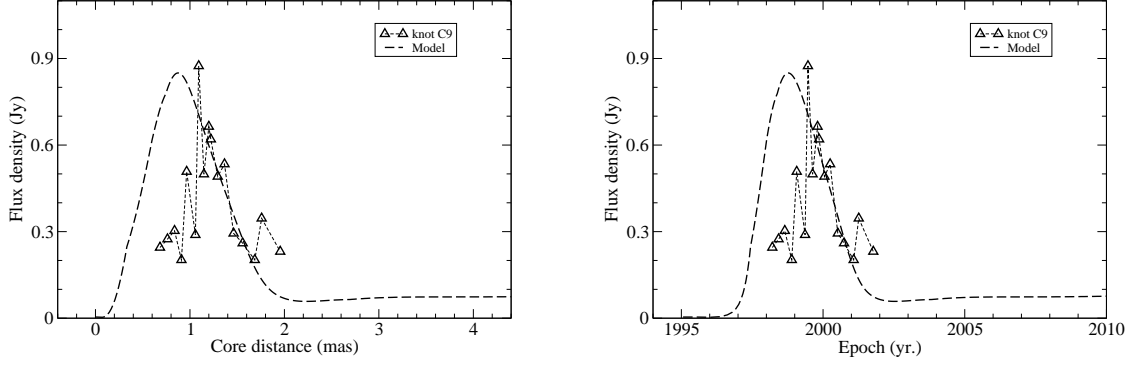


**Fig. 6.** Knot C9: The 43 GHz light curve  $S_{obs}(t)$  (shown by the triangles) as a function of core distance (left panel) and as a function of time (right panel) [the observational data are adopted from Jorstad et al. 2005]. The decaying part of the light curve is well fitted by the Doppler boosting profile predicted in our model-simulation of its kinematics (Qian 2022b).

trajectory are also pronounced for C9. Although the historically extrapolated position of C9 (using the average apparent speed of 15.6c) agrees well with the the measured position at epoch 1996.81 (Ros et al. 2000). It decelerates significantly from  $\sim 20c$  near the core to  $\sim 10c$  at 1 mas and then accelerates beyond 1.5 mas. The deceleration is accompanied by brightening of the knot and rotation of the EVPA by  $\sim 50^\circ$ , making it almost perpendicular to the jet direction.

It is worth noticing that the rapid variations in its intrinsic flux density (or the steepening of the local spectrum at 43 GHz) resulted in the peaking stage of the flare not observed at 43 GHz. Detailed model-fits to the light curves measured by Schinzel (2011a) at 15, 22 and 43 GHz will be presented below in Figure 7.

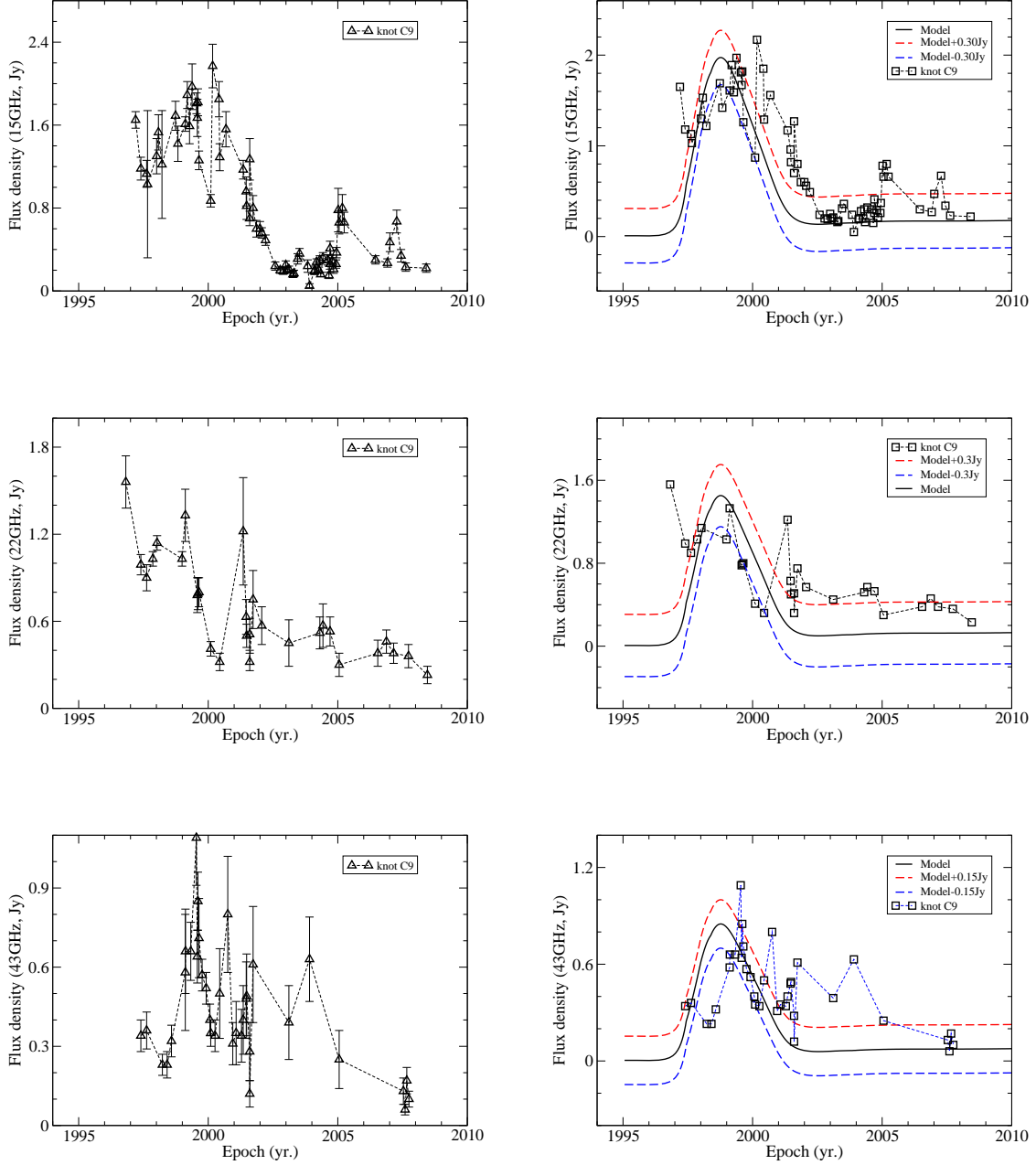
- It should be emphasized that the bulk Lorentz factor  $\Gamma(t)$ , viewing angle  $\theta(t)$  and Doppler factor  $\delta(t)$  as functions of time were directly derived from the model fitting of the kinematics only, and the Doppler boosting effect ( $[\delta(t)]^{3+\alpha}$ ) is purely predicted by the precessing nozzle scenario. Thus, whether the predicted Doppler boosting profile  $S_{int}[\delta(t)/\delta_{max}]^{3+\alpha}$  can explain the flux evolution of superluminal knots in 3C345 would be a significant test for our precessing nozzle scenario. In the model-simulation the intrinsic flux density  $S_{int}$  were adopted to be 3.83, 2.58 and 1.65  $\mu\text{Jy}$  for 15, 22 and 43 GHz, respectively. The spectral index was adopted as  $\alpha(15\text{-}22\text{-}43\text{GHz})=0.80$  ( $S_\nu \propto \nu^{-\alpha}$ ).
- The light curves observed at 15, 22 and 43 GHz for knot C9 <sup>1</sup> are shown in Figure 7 (left panels). They exhibit very complicated structures with flux density fluctuations on short time-scales of  $\sim 0.5$  years, but the Doppler boosting effect having a time scale of  $\sim 5$  years (1996.5–2001.5) as predicted by our model-simulation can be explicitly discerned: (1) During both the rising ( $\sim 1997.0\text{--}1998.5$ ) and decaying ( $\sim 1999.5\text{--}2001.0$ ) stages the flux densities measured at 15 GHz are well fitted by the Doppler boosting profiles (solid black lines in

Fig.7, right panels). Thus the model-predicted Doppler-boosting profiles can be regarded as correctly determined with its maximum at 1998.77, where the apparent speed and viewing angle are at minimum; (2) At both 22 and 43 GHz there are a few data-points are also fitted by the profiles during the rising satge ( $\sim 1997\text{--}1998$ ); (3) The low flux densities measured at 43 GHz during 1998–1999 and measured at 22 GHz during the decaying stage (1999.5–2000.5) are obviously due to the intrinsic variations of knot C9. For example, during 1998–1999 the measured spectral index  $\alpha(15\text{-}43\text{GHz})\sim 1.8$  much larger than that ( $\alpha(15\text{-}43\text{GHz})\sim 0.80$ ) during both rising and decaying stages; (4) The fluctuations on time-scales of 0.5–1 years in flux density measured at 15, 22 and 43 GHz during 2001–2008 can also be interpreted in terms of the intrinsic variations of knot C9, because the Doppler boosting effect has diminished during that period. Thus in order to fully explain the flux evolution of superluminal components in 3C345 both intrinsic variations and Doppler boosting effect should be taken into account; (5) In Figure 7 (right panels) the dashed red and blue lines show the profiles deviating from the model-derived Doppler boosting profiles (solid lines in black) by  $\pm 0.15$  Jy (for 43 GHz) and 0.30 Jy (for 22 and 15 GHz). It can be seen that most of the measured data-points fall between the two lines, indicating that the model-fits to the measured light curves are successful.

The brief summary described above for the midel-fitting results of the kinematic behavior and flux evolution for the superluminal components of jet-A in 3C345 explicitly shows that our processing nozzle scenario is most appropriate and valid to explain the kinematic, dynamic and emission properties observed in the superluminal components of blazar 3C345.

In the following we shall investigate the flux evolution associated with the Doppler boosting effect for five superluminal knots (C19, C20, C21, B5 and B7) belonging to the jet-B of 3C345. As in the previous work (Qian 2022b) the observational data are adopted from Schinzel (2011a) and Jorstad et al. (2005).

<sup>1</sup> Data are adopted from Schinzel (2011a) only.



**Fig. 7.** Knot C9: The light curves measured at 15, 22 and 43 GHz (left panels) and the model fits (right panels) in terms of their Doppler boosting effect ( $S_{obs}(t) = S_{int}[\delta(t)]^{3+\alpha}$  with  $\alpha(15\text{-}22\text{-}43\text{GHz}) = 0.80$ ;  $S_{\nu} \propto \nu^{-\alpha}$ ). All the three light curves are reasonably well fitted by the model-predicted Doppler boosting profiles (solid black lines), except some isolated spikes of short-time scales ( $\leq 0.5$  yr) which may be caused by the variations in the intrinsic flux density of knot C9 itself. The intrinsic flux densities were adopted as  $S_{int} = 3.83, 2.58$  and  $1.65 \mu\text{Jy}$  at 15, 22 and 43 GHz, respectively. The dashed red and blue lines (right panels) represent the profiles which deviate from the Doppler boosting profiles by  $\pm 0.30$  Jy (for the 22 and 15 GHz curves) and  $\pm 0.15$  Jy (for the 43 GHz curve), demonstrating that most of the measured data-points are fitted between the two lines and the observed light curves are reasonably well fitted. In addition, there are several isolated spikes on short time-scales during 2000–2008 superimposed on the regular variations. These spikes may be explained in terms of the variations in the intrinsic flux density and spectral index of knot C9 (a traveling shock or plasmoid).

## 2. Geometry and model parameters

According to the precessing nozzle scenario proposed for 3C345 (Qian 2022a, 2022b) the superluminal knots could be separated into two groups (group-A and group-B) which

were hypothetically assumed to be related to a double-jet structure (jet-A plus jet-B), because the two jets were found to be precessing with the same period of 7.3 yr, but having different patterns of precessing common trajectory. The geometry and model-parameters describing the

precessing nozzle scenario proposed for 3C345 have been discussed in detail in the previous works (Qian 2022a, 2022b). Here we only list the main points of the scenario related to the investigation of the kinematics of the superluminal knots of group-B as follows:

(1) Jet-axis

The direction of the axis of jet-B in space, around which superluminal knots of group-B move, is defined by parameters  $\epsilon$  and  $\psi$ . The jet-axis is assumed as:

$$x_0 = p(z_0)z_0^\zeta \quad (1)$$

where  $\epsilon=1.5^\circ$ ,  $\psi=12.0^\circ$ ,  $\zeta=1.0$  and  $p=1.34 \times 10^{-4}$  are adopted.

(2) Amplitude and phase of trajectory

The amplitude and phase of the trajectory of superluminal knots are defined as:

$$A(Z) = A_0[\sin(\pi Z/Z_1)] \quad (2)$$

$$\phi(Z) = \phi_0 \quad (3)$$

where  $A_0$  represents the amplitude coefficient of the common trajectory pattern.  $A_0=1.09$  mas and  $Z_1=396$  mas are adopted.  $\phi_0$  is the precession phase of an individual knot, which is related to its ejection time  $t_0$ :

$$\phi_0(\text{rad}) = 5.70 + \frac{2\pi}{T_0}(t_0 - 2002.12) \quad (4)$$

where  $T_0$  is the precession period of the jet nozzle.

The distribution of the precessing trajectories of the knots is shown in Figure 8, displaying a bunch of straight-line trajectories, which is completely different from that of the curved trajectories of the knots in jet-A.

(3) Doppler boosting effect

In order to investigate the relation between the flux evolution of superluminal components and their Doppler boosting effect during their accelerated/decelerated motion and model-fitting of the measured light curves, we define the Doppler boosting profile as  $S_{int}[\delta(t)]^{3+\alpha}$  or  $[\delta(t)/\delta_{max}]^{3+\alpha}$ , where  $S_{int}$ —the intrinsic flux density of the knot,  $\delta(t)$ —Doppler factor and  $\alpha$ —spectral index (in the frequency range of 10.7–43 GHz). The observed flux density  $S_{obs}(\nu, t)$  of the superluminal components is Doppler-boosted:

$$S_{obs}(\nu, t) = S_{int}(\nu) \times \delta(t)^{3+\alpha} \quad (5)$$

$S_{int}(\nu)=S_0(\nu/\nu_0)^{-\alpha}$ ,  $S_0$ —the flux density at the fiducial frequency  $\nu_0$ .<sup>2</sup>

(4) Cosmological model

<sup>2</sup> Here in this paper we assume  $S_{int}$  and  $\alpha$  are constants, not depending on time and frequency. In general case both  $S_{int}$  and  $\alpha$  could be defined as functions of frequency and time. Thus flux evolution of superluminal knots would be associated with more complex Doppler-boosting effect.

We will apply the concordant cosmological model (Spergel et al. 2003, Hogg 1999) with  $\Omega_\lambda=0.73$  and  $\Omega_m=0.27$ , and  $H_0=71 \text{ km s}^{-1} \text{ Mpc}^{-1}$ . Thus the luminosity distance of 3C345  $D_L=3.49$  Gpc, the angular-diameter distance  $D_a=1.37$  Gpc,  $1 \text{ mas}=6.65 \text{ pc}$  and  $1 \text{ mas/yr}=34.6 \text{ c}$ .  $1 \text{ c}$  is equivalent to an angular speed  $0.046 \text{ mas/yr}$  in the rest frame.

### 3. Knot C19: Interpretation of kinematics and flux evolution

According to the precessing nozzle scenario for jet-B, knot C19 has its ejection time  $t_0=2004.85$  and corresponding precession phase  $\phi_0=1.77+2\pi$ . Its traveled distance  $Z(t)$  and parameters  $\epsilon(t)$  and  $\psi(t)$  are model-fitted as shown in Figure 9. Before 2008.87  $\epsilon=1.50^\circ$  and  $\psi=12.0^\circ$ , knot C9 moved along the precessing common trajectory. The corresponding traveled distance  $Z=14.6 \text{ mas}=97.1 \text{ pc}$ . After 2008.87 (core separation  $r_n>0.26 \text{ mas}$  or  $X_n>0.25 \text{ mas}$ )  $\epsilon$  and  $\psi$  started to change and knot C19 started to move along its own individual track, deviating from the precessing common track.

#### 3.1. Knot C19: Model simulation of kinematics

The model-fitting results of the entire trajectory  $Z_n(X_n)$ , core separation  $r_n(t)$  and coordinates  $X_n(t)$  and  $Z_n(t)$  for knot C19 are shown in Figures 10 and 11. They are all well fitted because the transition between the common track in the inner jet region and the individual track in the outer jet region has been taken into account.

The model-derived apparent speed  $\beta_{app}(t)$  and viewing angle  $\theta(t)$  as continuous functions of time are shown in Figure 12 (right panel):  $\beta_{app}(t)$  has a prominent bump during 2007.5–2008.8 with its peak of 6.57 (at 2008.22), while  $\theta(t) \simeq 1.0^\circ$ . The modeled bulk Lorentz factor  $\Gamma(t)$  and Doppler factor  $\delta(t)$  as continuous functions of time are shown in Figure 12 (left panel), also demonstrating a distinct bump structure with  $\Gamma_{max}=14.8$  and  $\delta_{max}=26.3$ .

#### 3.2. Knot C19: Doppler boosting effect and flux evolution

The light curve observed at 43 GHz and its corresponding normalized light curve are well fitted (Figure 13) in terms of the Doppler boosting profile  $S_{int}[\delta(t)]^{3+\alpha}$  and  $[\delta(t)/\delta_{max}]^{3+\alpha}$ , respectively. A spectral index  $\alpha=0.40$  and an intrinsic flux density  $S_{int}=10.8 \mu\text{Jy}$  are adopted.

### 4. Knot C20: Interpretation of kinematics and flux evolution

According to the precessing nozzle scenario for jet-B, the ejection time of knot C20 is  $t_0=2007.68$  and corresponding precession phase  $\phi_0=4.20+2\pi$ . Its traveled distance  $Z(t)$  and parameters  $\epsilon(t)$  and  $\psi(t)$  were model-fitted as functions of time as shown in Figure 14. Before 2008.66  $\epsilon=1.50^\circ$  and  $\psi=12.0^\circ$ , knot C20 moved along the precessing common trajectory. The corresponding traveled distance  $Z=4.0 \text{ mas}=26.6 \text{ pc}$ . After 2008.66 (core separation  $r_n>0.14 \text{ mas}$  or coordinate  $X_n>0.13 \text{ mas}$ ) parameter  $\epsilon$  started to change (parameter  $\psi$  started to change after

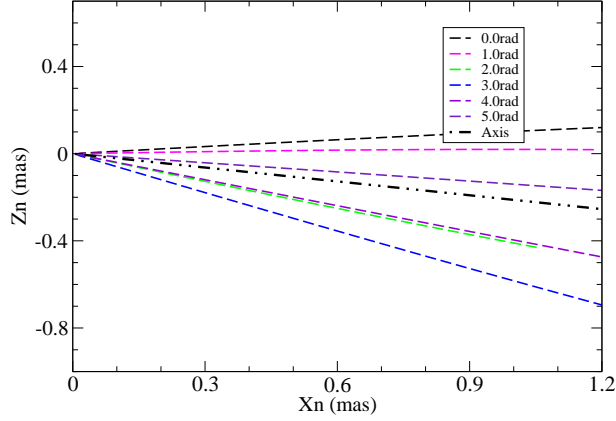


**Fig. 8.** Jet B: Distribution of the precessing trajectories for precession phases  $\phi_0=0.0, 1.0, 2.0, 3.0, 4.0$  and  $5.0$  rad. The jet axis is at position angle  $-102^\circ$ . This distribution modeled for jet-B is like a bunch of straight-line tracks, which is completely different from that of the curved trajectories caused by the helical pattern of precessing common trajectory assumed for jet-A. This distribution illustrates both the swing of the ejection position angle and the apparent tracks of superluminal knots in jet-B ejected at different precession phases. Jet-B consists of 14 components: C15, C15a, C16 to C21, B5 to B8, B11 and B12 (Qian 2022a).

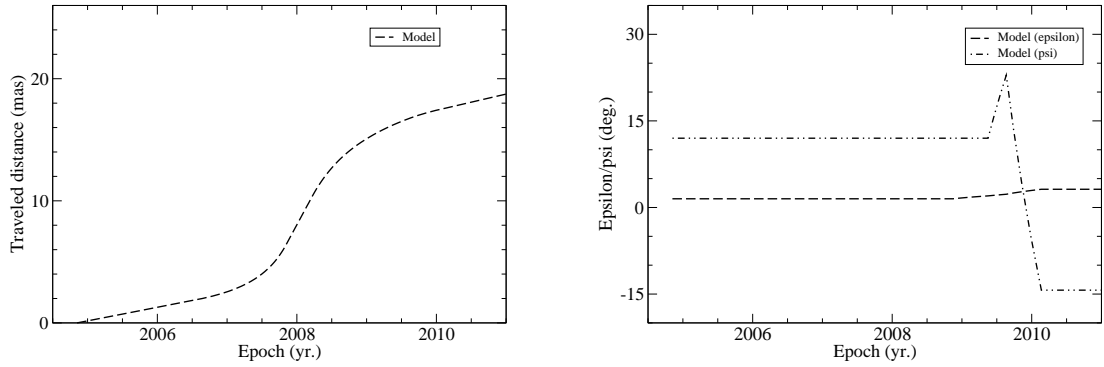


**Fig. 9.** Knot C19: Model-derived traveled distance  $Z(t)$ , parameters  $\epsilon(t)$  and  $\psi(t)$ . Before 2008.87 ( $X_n \leq 0.25$  mas)  $\epsilon=1.5^\circ$  and  $\psi=12.0^\circ$ , knot C19 moved along the precessing common trajectory, while after 2008.87 ( $X_n > 0.25$  mas)  $\epsilon$  and  $\psi$  started to change, and knot C19 started to move along its own individual track, deviating from the precessing common track.

2009.4) and its motion started to follow its own individual track, deviating from the precessing common track.

#### 4.1. Knot C20: Model simulation of kinematics

The model-fitting results of the entire trajectory  $Z_n(X_n)$ , core distance  $r_n(t)$ , coordinates  $X_n(t)$  and  $Z_n(t)$  for knot C20 are presented in Figure 15 and Figure 16. They are all well fitted because the transition between the common track in the inner jet region and the individual track in the outer jet region has been considered. The model-derived apparent speed  $\beta_{app}(t)$  and viewing angle  $\theta(t)$  as continuous functions of time are shown in Figure 17 (left panel). The apparent speed has two peaks at 2008.66 and 2009.44:  $\beta_{app}=9.57$  and  $7.50$ , respectively. The corresponding viewing angles are  $\theta=1.95^\circ$  and  $1.03^\circ$ .

The model-derived bulk Lorentz factor  $\Gamma(t)$  and Doppler factor  $\delta(t)$  as continuous functions of time are shown in Figure 17 (right panel). Both have a peak at 2009.44, coincident with the second peak in the apparent speed:  $\Gamma_{max}=15.0$  and  $\delta_{max}=27.9$ .

#### 4.2. Knot C20: Doppler boosting effect and flux evolution

The model fitting of the measured 43 GHz light curve and its corresponding normalized light curve are shown in Figure 18. Both are well model-fitted in terms of the Doppler boosting effect with an assumed spectral index at 43 GHz of  $\alpha=0.70$  and an intrinsic flux density  $S_{int}=16.2 \mu\text{Jy}$ . The maximal flux density  $S_{max}=3.63 \text{ Jy}$  at 2009.44.



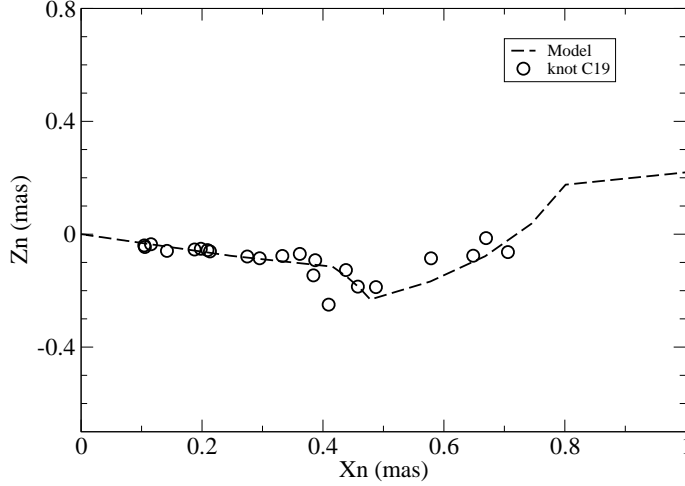


**Fig. 10.** Knot C19: Model fitting of the entire trajectory  $Z_n(X_n)$ . Within  $X_n=0.25$  mas knot C19 moved along the precessing common trajectory, while beyond that it started to move along its own individual track.

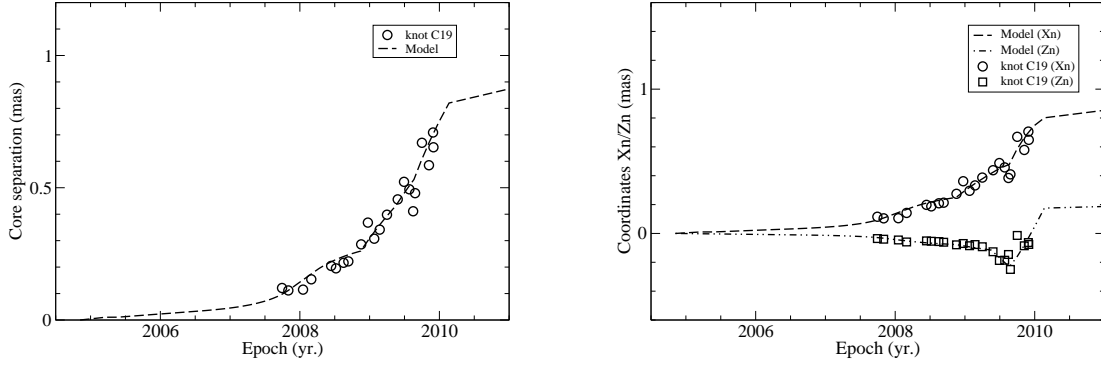


**Fig. 11.** Knot C19: Model fitting of the core separation  $r_n(t)$ , coordinates  $X_n(t)$  and  $Z_n(t)$ . Both the precessing common trajectory (inner track; before 2008.66,  $X_n \leq 0.25$  mas) and the individual trajectory (outer track; after 2008.66,  $X_n > 0.25$  mas) are well fitted.

## 5. Knot C21: Interpretation of kinematics and flux evolution

According to the precessing nozzle scenario for jet-B the ejection time of knot C21 is  $t_0=2007.32$  and the corresponding precession phase  $\phi_0=3.90+2\pi$ . Its traveled distance  $Z(t)$  and modeled parameters  $\epsilon(t)$  and  $\psi(t)$  as continuous functions of time are shown in Figure 19. Before 2009.08  $\epsilon=1.50^\circ$  and  $\psi=12.0^\circ$ , knot C21 moved along the precessing common track, which extends to the traveled distance  $Z=3.40$  mas=22.6 pc. After 2009.08 ( $r_n \geq 0.11$  mas or  $X_n \geq 0.10$  mas) parameter  $\epsilon$  started to change (parameter  $\psi$  started to change after 2009.40) and knot C21 started to follow its own individual track, deviating from the precessing common track. That is, the transition between the precessing common track and its individual track occurred at  $X_n \sim 0.10$  mas.

### 5.1. Knot C21: model simulation of kinematics

The model-fitting results of the entire trajectory  $Z_n(X_n)$ , and the core separation  $r_n(t)$  and coordinates  $X_n(t)$  and  $Z_n(t)$  as functions of time are shown in Figures 20 and 21. They are all well fitted in both inner and outer jet regions. The model-derived apparent speed  $\beta_{app}(t)$  and viewing angle  $\theta(t)$  as functions of time are shown in Figure 22 (right panel), Both exhibit three peaks at 2009.33, 2009.56 and 2009.76 with  $\beta_{app}=10.9, 8.4$  and  $10.2$ , respectively. The corresponding viewing angles are  $\theta=1.32^\circ, 1.04^\circ$  and  $1.20^\circ$ , respectively.

The model-derived bulk Lorentz factor  $\Gamma(t)$  and Doppler factor  $\delta(t)$  as continuous functions of time are shown in Figure 22 (left panel). Both also show three peaks at 2009.40, 2009.56 and 2009.76 with  $\Gamma=16.50, 15.87$  and  $16.46$ , respectively. The corresponding Doppler factor  $\delta=29.43, 29.29$  and  $29.38$ , respectively. These peaks are well coincident with the peaks in the measured light curve.

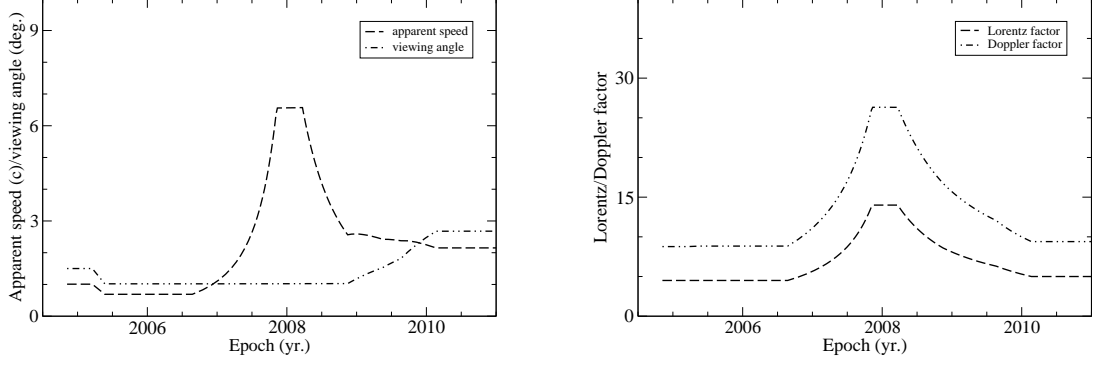


**Fig. 12.** Knot C19. Left panel: the model-derived apparent speed  $\beta_{app}(t)$  and viewing angle  $\theta(t)$  as functions of time. The apparent speed has a maximum  $\beta_{app}(t)=6.57$  at 2008.22 and the viewing angle  $\theta(t)\simeq 1.02^\circ$  during 2007.5–2008.8. Right panel: the model-derived bulk Lorentz factor  $\Gamma(t)$  and Doppler factor  $\delta(t)$  as functions of time. During 2007.86–2008.22  $\Gamma(t)=18.40$  and  $\delta(t)\simeq 26.32$  (a maximum).

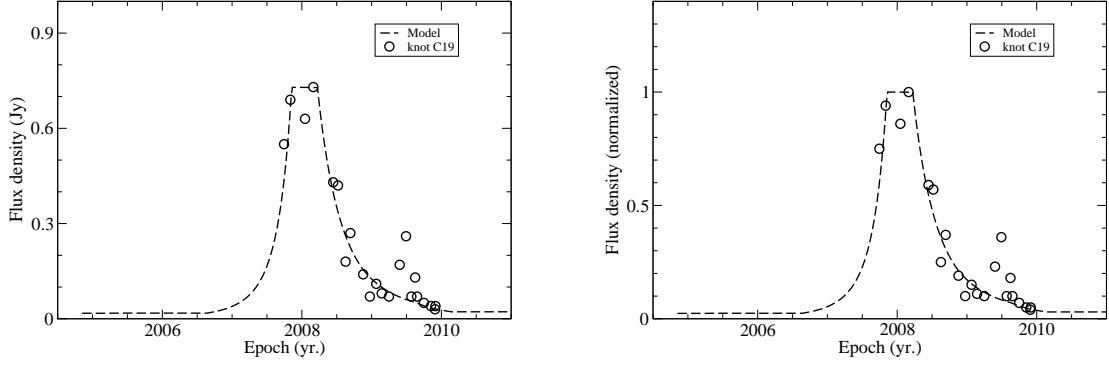


**Fig. 13.** Knot C19: Model fitting of the 43GHz light curve (left panel) and its corresponding normalized light curve (right panel). Both are very well fitted by the Doppler boosting profile  $S_{int}[\delta(t)]^{3+\alpha}$  and  $[\delta(t)/\delta_{max}]^{3+\alpha}$ , respectively. An intrinsic flux density  $S_{int}=10.8\mu\text{Jy}$  and a spectral index  $\alpha=0.40$  are adopted.

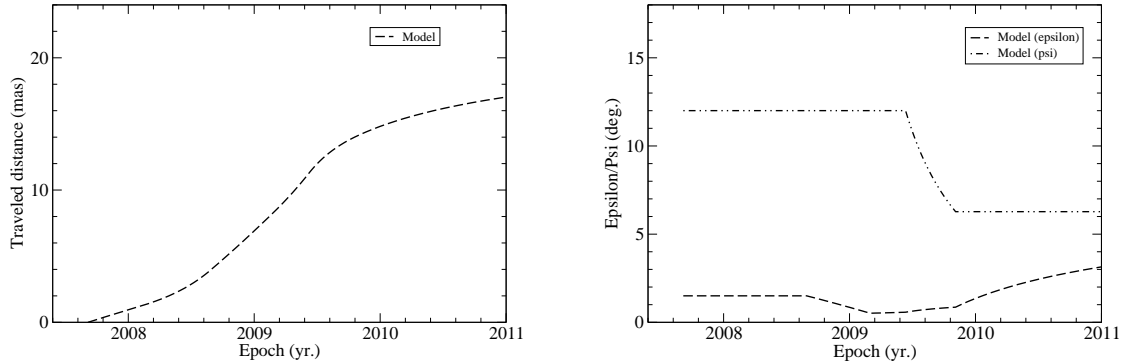


**Fig. 14.** Knot C20: The model-derived traveled distance  $Z(t)$  (left panel), parameters  $\epsilon(t)$  and  $\psi(t)$  (right panel). Before 2008.66 ( $X_n < 0.13$  mas)  $\epsilon=1.50^\circ$  and  $\psi=12.0^\circ$  knot C20 moved along the precessing common trajectory. The corresponding traveled distance extends to  $Z=4.0$  mas = 26.6 pc. After 2008.66  $\epsilon$  started to change ( $\psi$  started to change after 2009.44) and knot C20 started to move along its own individual track. That is, the transition from the precessing common track to its individual track occurred at 2008.66.

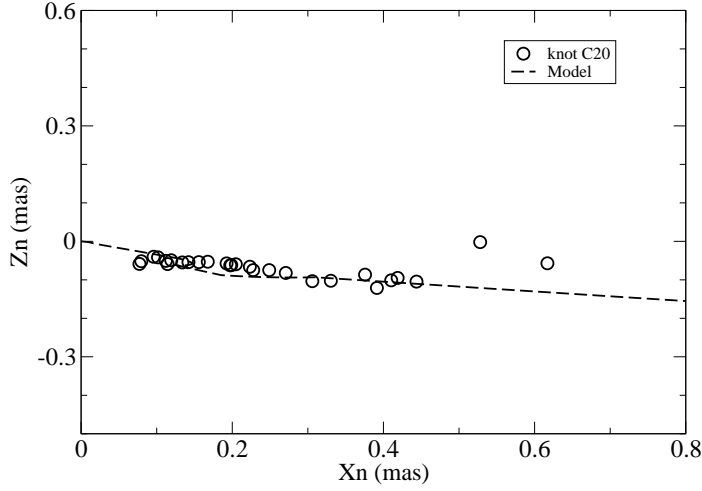


**Fig. 15.** Knot C20: Model-fitting of the entire trajectory  $Z_n(X_n)$ . Within  $X_n=0.13$  mas, knot C20 moved along the precessing common track and beyond  $X_n=0.13$  mas it started to move along its own individual track. Thus transition from the precessing common track to its own individual track occurred at  $X_n=0.13$  mas.

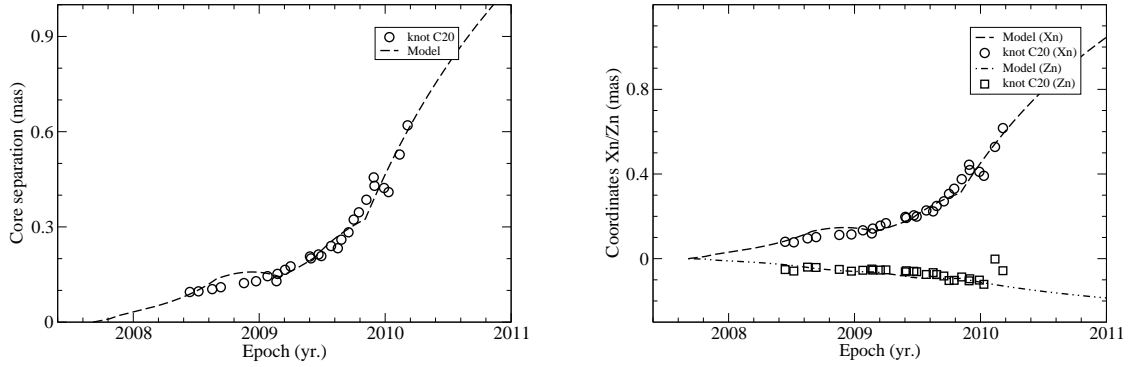


**Fig. 16.** Knot C20: Model fitting of the core separation  $r_n(t)$ , coordinates  $X_n(t)$  and  $Z_n(t)$ . Both the inner precessing common track ( $X_n \leq 0.13$  mas) and the outer individual track ( $X_n > 0.13$  mas) are well fitted.

### 5.2. Knot C21: Doppler boosting effect and flux evolution

The model fitting results of the measured 43 GHz light curve and its corresponding normalized light curve are shown in Figure 23. It can be seen that the entire light curve with three peaks (2.62 Jy at 2009.40, 2.57 Jy at 2009.56 and 2.61 at 2009.76) is very well fitted in terms of the model-derived Doppler boosting profile with an assumed spectral index  $\alpha=0.70$  and an intrinsic flux density  $S_{int}=9.64\mu\text{Jy}$ , indicating that the modeled Doppler boosting effect may dominate the complex flaring event and the intrinsic emission of knot C21 is quite stable.

## 6. Knot B5: Interpretation of kinematics and flux evolution

According to the precessing nozzle scenario for jet-B the ejection time of knot B5 is  $t_0=2010.48$  and the corresponding precession phase  $\phi_0=0.33+4\pi$ . Its traveled distance  $Z(t)$

and modeled parameters  $\epsilon(t)$  and  $\psi(t)$  as functions of time are shown in Figure 24. Before 2010.88 ( $X_n \leq 0.015$  mas)  $\epsilon=1.50^\circ$  and  $\psi=12.0^\circ$  knot B5 moved along the precessing common trajectory which extends to the traveled distance  $Z=0.60$  mas = 4.0 pc. After that epoch both  $\epsilon$  and  $\psi$  started to change and knot B5 started to follow its own individual track, deviating from the precessing common track. That is, the transition between the precessing common track and its individual track occurred very near to the core (at  $r_n \sim X_n = 0.015$  mas) and the Doppler-boosting effect occurred completely in the outer jet regions.

### 6.1. Knot B5: Model simulation of kinematics

The model-fitting results of the entire trajectory  $Z_n(X_n)$  and the core separation  $r_n(t)$ , coordinates  $X_n(t)$  and  $Z_n(t)$  as functions of time are shown in Figures 25 and 26. They are all well fitted during the five years ( $\sim 2011.0$ –2016.0).

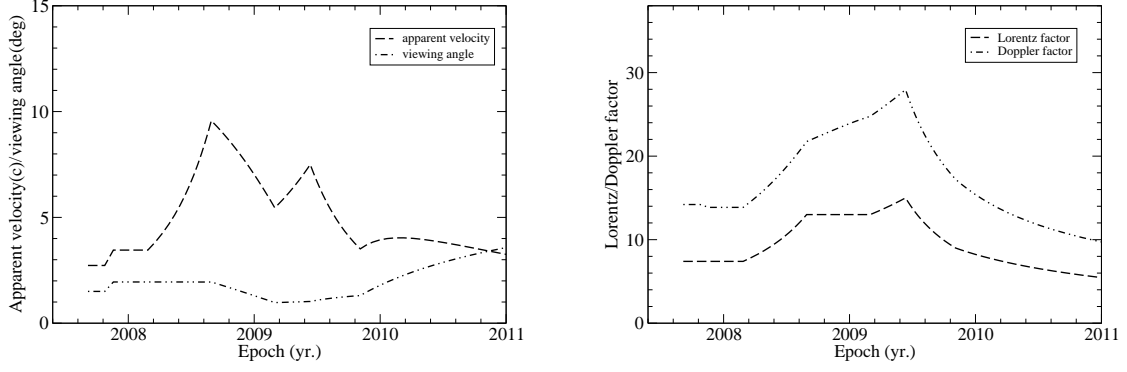


**Fig. 17.** Knot C20. Left panel: the model-derived apparent speed  $\beta_{app}(t)$  and viewing angle  $\theta(t)$  as functions of time. The apparent speed has two peaks:  $\beta_{app}=9.57$  at 2008.66 and 7.50 at 2009.44. The corresponding viewing angles are  $\theta=1.95^\circ$  and  $=1.03^\circ$ , respectively. Right panel: the model-derived bulk Lorentz factor  $\Gamma(t)$  and Doppler factor  $\delta(t)$ . Both have a peak  $\Gamma_{max}=15.00$  and  $\delta_{max}=27.95$  at 2009.44, coincident with the second peak in the apparent speed  $\beta_{app}$ .

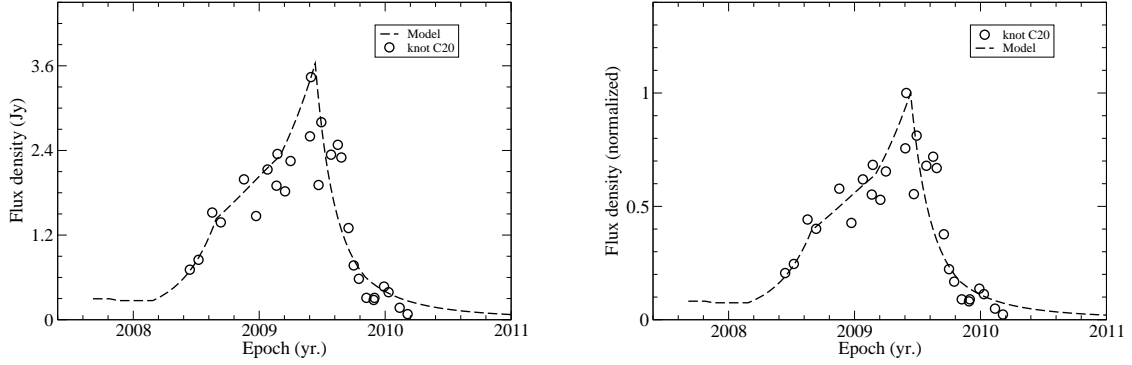


**Fig. 18.** Knot C20: model fitting of the 43 GHz light curve (left panel) and its corresponding normalized light curve (right panel). They are well fitted by the Doppler boosting profile  $S_{int}[\delta(t)]^{3+\alpha}$  and  $[\delta(t)/\delta_{max}]^{3+\alpha}$ , respectively. An intrinsic flux density  $S_{int}=16.2 \mu\text{Jy}$  and a spectral index  $\alpha=0.70$  are adopted.

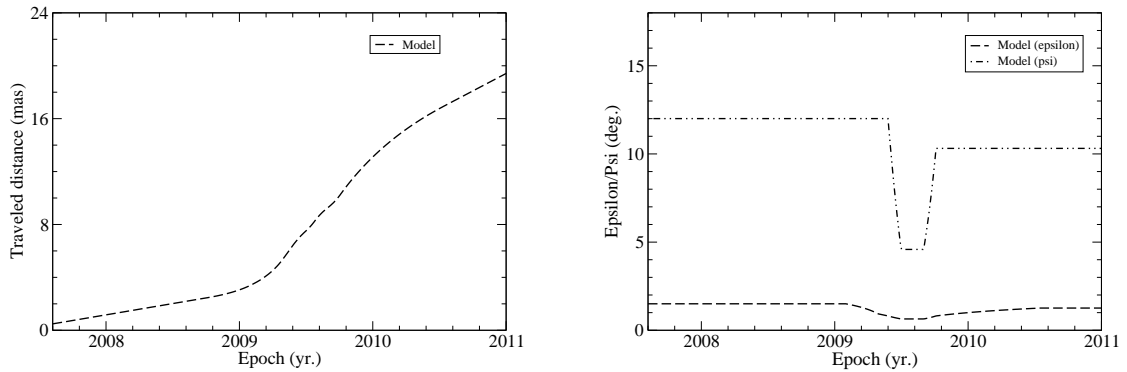


**Fig. 19.** Knot C21: The model-derived traveled distance  $Z(t)$ , parameters  $\epsilon(t)$  and  $\psi(t)$  as functions of time. Before 2009.08 ( $X_n \leq 0.10 \text{ mas}$ )  $\epsilon=1.50^\circ$  and  $\psi=12.0^\circ$ , knot C21 moved along the precessing common trajectory, while after 2009.08 ( $X_n > 0.10 \text{ mas}$ )  $\epsilon$  started to change ( $\psi$  started to change after 2009.40), knot C21 started to move along its own individual track, deviating from the precessing common track. Thus the transition from the precessing common track to its own individual track occurred at  $X_n=0.10 \text{ mas}$ . The corresponding traveled distance is  $Z=3.40 \text{ mas}=22.6 \text{ pc}$ .

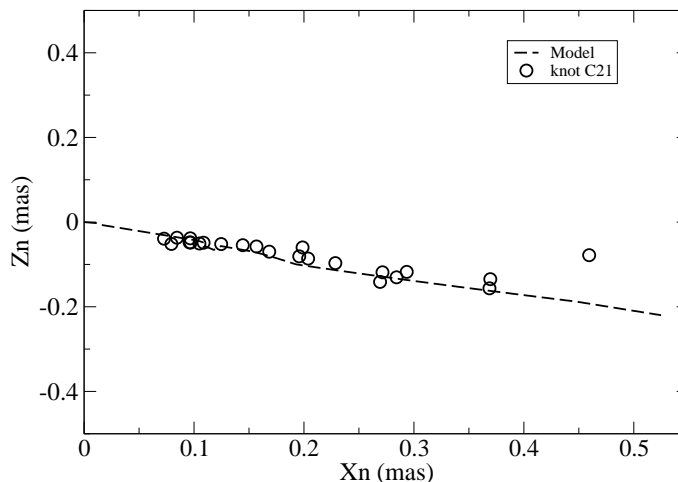


**Fig. 20.** Knot C21: Model fitting of the entire trajectory  $Z_n(X_n)$ . Within  $X_n=0.10$  mas knot C21 moved along the precessing common trajectory, while beyond  $X_n=0.10$  mas it started to move along its own individual track. Both the inner precessing common track and the outer individual track are well fitted.

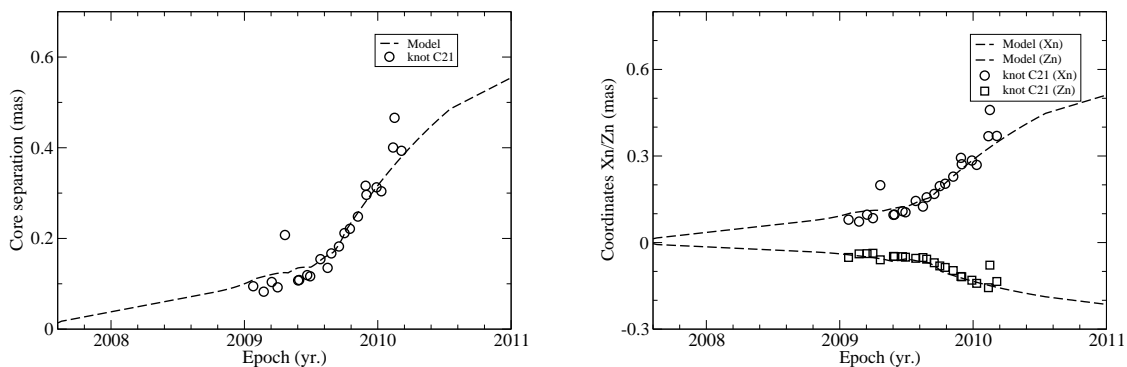


**Fig. 21.** Knot C21: Model fitting of the core separation  $r_n(t)$ , coordinates  $X_n(t)$  and  $Z_n(t)$  as functions of time. They are all well fitted.

The rapid increase in core distance  $r_n$  during  $\sim 2012.8$ – $2014.0$  was mostly induced by the increase in the viewing angle  $\theta$ .

The model-derived apparent velocity  $\beta_{app}(t)$  and viewing angle  $\theta(t)$  as continuous functions of time are shown in Figure 27 (left panel). The maximal apparent speed  $\beta_{app,max}=16.54$  occurred at 2011.28 and the corresponding viewing angle  $\theta=2.53^\circ$ ,  $\Gamma=17.2$  and  $\delta=21.81$ .

The model-derived bulk Lorentz factor  $\Gamma(t)$  and Doppler factor  $\delta(t)$  as continuous functions of time are shown in Figure 27 (right panel). The maximal Lorentz factor  $\Gamma_{max}=17.20$  (during 2011.13–2011.28). The maximal Doppler factor  $\delta_{max}=25.21$  at 2011.13 and the corresponding viewing angle  $\theta=2.01^\circ$  (a local minimum).

### 6.2. Knot B5: Doppler boosting effect and flux evolution

The model fitting results of the measured 43 GHz light curve and its corresponding normalized light curve are

shown in Figure 28. The light curve of the radio burst measured during 2011–2011.4 is well fitted in terms of the Doppler boosting effect with an assumed spectral index  $\alpha=0.50$  and an intrinsic flux density  $S_{int}=12.9 \mu\text{Jy}$ . The flux fluctuations observed during  $\sim 2012.2$ – $2014.2$  may be due to the variations in the intrinsic flux density of knot B5.

### 7. Knot B7: Interpretation of kinematics and flux evolution

According to the precessing nozzle scenario for jet-B the ejection time of knot B7 is  $t_0=2011.60$  and its corresponding precession phase  $\phi_0=1.30+4\pi$ . Its traveled distance  $Z(t)$  and the modeled parameters  $\epsilon(t)$  and  $\psi(t)$  as functions of time are shown in Figure 29. Before 2012.60 ( $X_n \leq 0.036$  mas)  $\epsilon=1.50^\circ$  and  $\psi=12.0^\circ$  knot B7 moved along the precessing common trajectory, extending to the traveled distance  $Z=2.0$  mas = 13.3 pc. After 2012.60 both

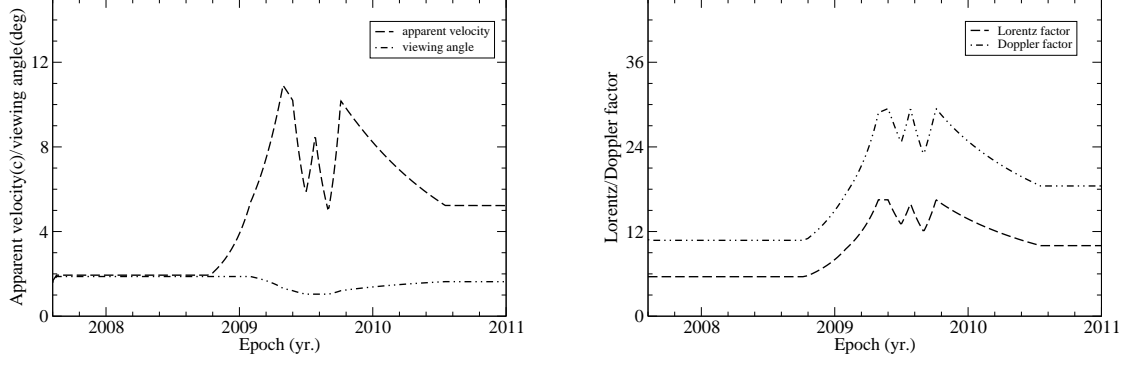


**Fig. 22.** Knot C21. Left panel: the model-derived apparent speed  $\beta_{app}(t)$  and viewing angle  $\theta(t)$  as functions of time. The apparent speed has three peaks  $\beta_{app} = 10.91, 8.43$  and  $10.16$  at  $2009.33, 2009.56$  and  $2009.76$ , respectively. The corresponding viewing angles are  $\theta = 1.32^\circ, 1.04^\circ$  (a minimum) and  $1.21^\circ$ , respectively. Right panel: the model-derived bulk Lorentz factor  $\Gamma(t)$  and Doppler factor  $\delta(t)$  as continuous functions of time. The Doppler factor has three peaks  $\delta = 29.43$  (at  $2009.40$ ),  $29.29$  (at  $2009.56$ ) and  $29.38$  (at  $2009.76$ ). The corresponding bulk Lorentz factor  $\Gamma = 16.50, 15.88$  and  $15.87$ , respectively.

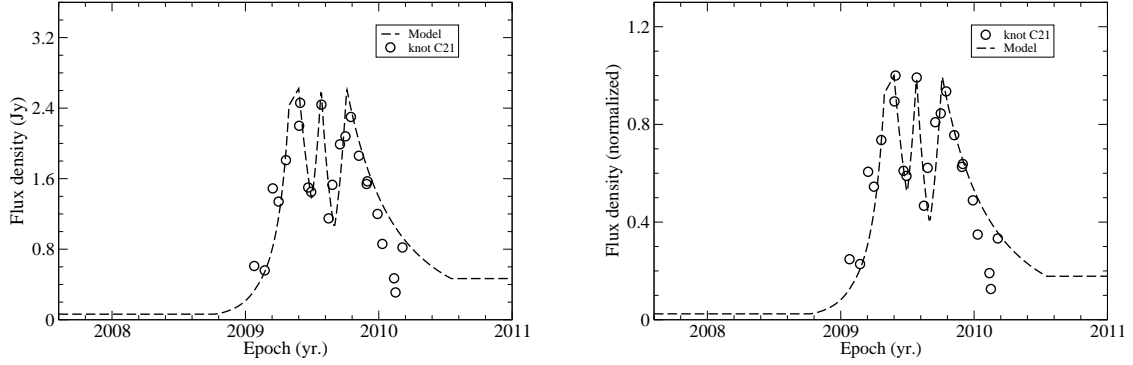


**Fig. 23.** Knot C21: Model fitting of the 43 GHz light curve (left panel) and its corresponding normalized light curve (right panel). Both are well fitted by the model-derived Doppler boosting profile  $S_{int}[\delta(t)^{3+\alpha}]$  and  $[\delta(t)/\delta_{max}]^{3+\alpha}$ , respectively. An intrinsic flux density  $S_{int} = 9.64 \mu\text{Jy}$  and a spectral index  $\alpha = 0.70$  are adopted. The modeled peak flux densities are  $2.62 \text{ Jy}$  (at  $2009.40$ ),  $2.57 \text{ Jy}$  (at  $2009.56$ ) and  $2.61 \text{ Jy}$  (at  $2009.76$ ), respectively.

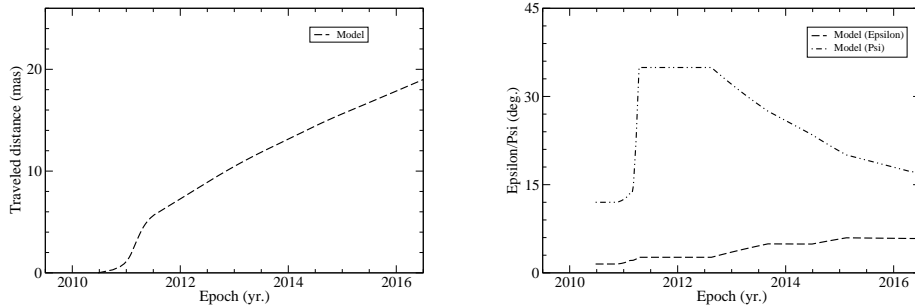


**Fig. 24.** Knot B5: The modeled traveled distance  $Z(t)$ , parameters  $\epsilon(t)$  and  $\psi(t)$  as functions of time. Before  $2010.88$   $\epsilon = 1.50^\circ$  and  $\psi = 12.0^\circ$ , knot B5 moved along the precessing common trajectory, while after that epoch both  $\epsilon$  and  $\psi$  started to change and knot B5 started to move along its own individual track, deviating from the common track. Thus the transition from the precessing common track to its own individual track occurred at  $\sim 2010.88$  ( $X_n = 0.015 \text{ mas}$ ), corresponding to a traveled distance  $Z = 0.6 \text{ mas} = 4.0 \text{ pc}$ . Only its individual track in the outer jet region was observed.

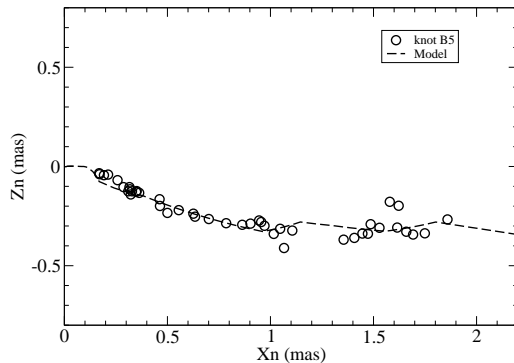


**Fig. 25.** Knot B5: Model fitting of the entire trajectory  $Z_n(X_n)$ . Within  $X_n=0.015$  mas knot B5 moved along the precessing common trajectory (with a precession phase  $\phi_0=0.33+4\pi$ ), while beyond  $X_n=0.015$  mas it started to move along its own individual track. The entire trajectory is very well fitted, but only its individual track in the outer jet region was observed.

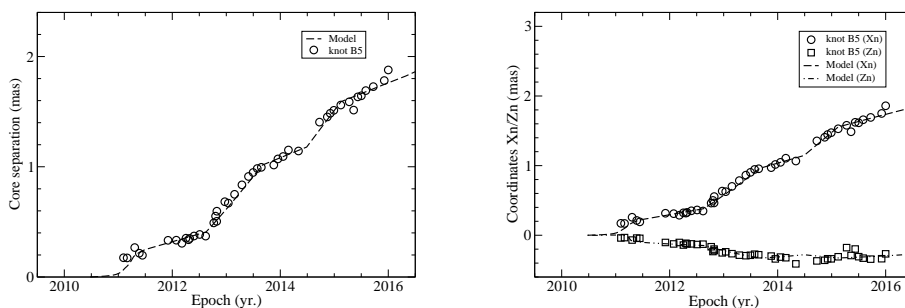


**Fig. 26.** Knot B5: Model fitting of the core separation  $r_n(t)$ , coordinates  $X_n(t)$  and  $Z_n(t)$  as functions of time. They are all well fitted. Only its individual track in the outer jet region (after 2010.88,  $X_n \geq 0.015$  mas) was observed.

parameters started to change and knot B7 started to move along its own individual track, deviating from the precessing common track. That is, the transition from the common track to its individual track occurred at  $r_n \sim X_n = 0.036$  mas. Thus its flaring associated with the Doppler boosting effect completely occurred in the outer jet region.

### 7.1. Knot B7: Model simulation of kinematics

The model fitting results of the entire trajectory  $Z_n(X_n)$  and the core separation  $r_n(t)$ , coordinates  $X_n(t)$  and  $Z_n(t)$  as functions of time are shown in Figures 30 and 31. They are all well fitted during the four years (2013–2016), especially for the prominent decrease in the core distance  $r_n$  near epoch 2016.

The model-derived apparent speed  $\beta_{app}(t)$  and viewing angle  $\theta(t)$  as continuous functions of time are shown in Figure 32 (left panel). The maximal apparent speed  $\beta_{app,max}=15.15$  at 2013.30.

The model-derived bulk Lorentz factor  $\Gamma(t)$  and Doppler factor  $\delta(t)$  as continuous functions are shown in Figure 32 (right panel). The maximal Doppler factor  $\delta_{max}=27.16$  occurred at 2013.30, coincident with the maximal apparent speed. The corresponding Lorentz factor  $\Gamma=17.5$  (a maximum) and  $\theta=1.89^\circ$ .

### 7.2. Knot B7: Doppler boosting effect and flux evolution

The model fitting results of the measured 43 GHz light curve and its corresponding normalized light curve are shown in Figure 33. Both are well fitted by the Doppler-boosting profile  $S_{int}[\delta(t)]^{3+\alpha}$  and  $[\delta(t)/\delta_{max}]^{3+\alpha}$ , respectively. An intrinsic flux density  $S_{int}=28.0 \mu\text{Jy}$  and a spectral index  $\alpha=0.50$  are adopted.

## 8. Conclusion

Based on the precessing nozzle scenario proposed for jet-B in 3C345 (Qian 2022a) we have model-fitted the flux evolution of five superluminal components (C19, C20, C21, B5 and B7) associated with their kinematics (accelerated/decelerated motion). Combining with the results for the five superluminal knots (C4, C5, C9, C10 and C22) of jet-A (Qian 2022b), we have interpreted the flux evolution as caused by the Doppler boosting effect for ten superluminal knots in 3C345.

In fact, similar studies can be made for more superluminal knots in 3C345: e.g., knots C7, C11, C12 and C23 of jet-A and C15–C18, B8, B11 and B12 of jet-B.

In addition, we have also applied our precessing nozzle scenario to investigate the flux evolution of superluminal components associated with their Doppler boosting effect in

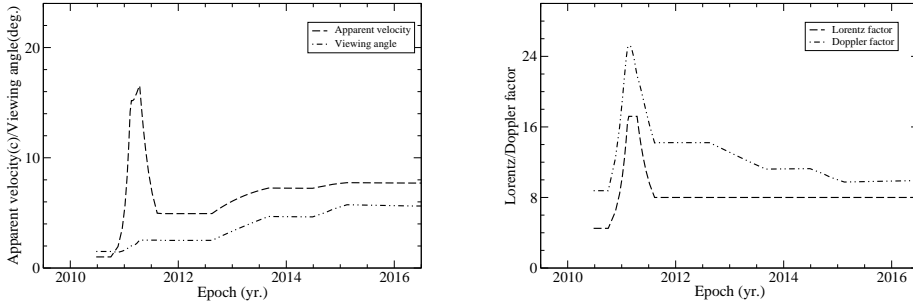


**Fig. 27.** Knot B5. Left panel: the model-derived apparent speed  $\beta_{app}(t)$  and viewing angle  $\theta(t)$  as functions of time. The apparent velocity has a maximum  $\beta_{app,max}=16.54$  at 2011.28 and the corresponding viewing angle  $\theta=2.53^\circ$ ,  $\Gamma=17.20$  and  $\delta=21.81$ . Right panel: the model-derived bulk Lorentz factor  $\Gamma(t)$  and Doppler factor  $\delta(t)$  as continuous functions of time. The Doppler factor has a maximum  $\delta_{max}=25.21$  at 2011.13 and the corresponding Lorentz factor  $\Gamma=17.20$  and viewing angle  $\theta=2.01^\circ$  (a local minimum). The Lorentz factor  $\Gamma=17.20$  (during 2011.13–2011.28, at maximum), coincident with the maximal Doppler factor.

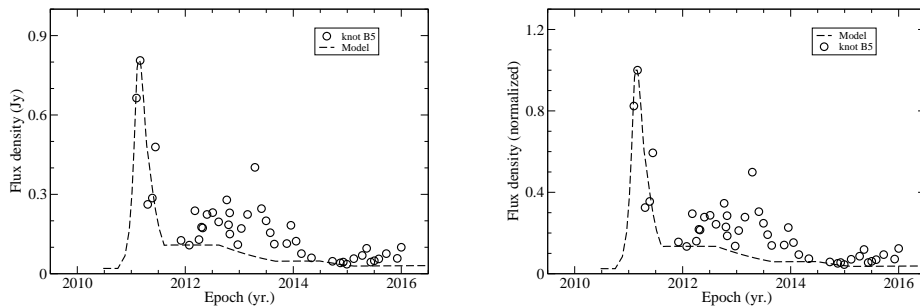


**Fig. 28.** Knot B5: Model fitting of the 43 GHz light curve (left panel) and its corresponding normalized light curve (right panel). Both are well fitted by the model-derived Doppler boosting profile  $S_{int}[\delta(t)]^{3+\alpha}$  and  $[\delta(t)/\delta_{max}]^{3+\alpha}$ , respectively. An intrinsic flux density  $S_{int}=12.9 \mu\text{Jy}$  and a spectral index  $\alpha=0.50$  were adopted. The rapid flux density fluctuations during 2012–2014 may be due to the variations in its intrinsic flux density and spectral index.

QSO B1308+326 (Qian 2023a) and blazars 3C454.3 (Qian 2023b) and 3C279 (Qian 2022b). In all these cases the flux evolution of the superluminal components can be interpreted in terms of their Doppler boosting effect combined with their intrinsic flux variations.

We would like to note that there are significant differences in the application of the precessing nozzle scenario to QSOs and blazars. For QSOs [e.g., for B1308+326 (Qian et al. 2017, Qian 2023a), PG1302-102 (Qian et al. 2018a) and NRAO 150 (Qian 2016)] the precessing nozzle scenario has been applied to study the model-fitting of the kinematics and flux evolution of superluminal components ejected from a single precessing jet, while for blazars [e.g., 3C345 (Qian 2022a, 2022b and this paper); 3C454.3 (Qian et al. 2007, 2014, 2021, Qian 2023b); 3C279 (Qian 2011, 2012, 2013, 2022a); OJ287 (Qian 2015, 2018b, 2019, 2020)] a double jet structure (jet-A plus jet-B) has been hypothetically introduced to study the kinematics and flux evolution of their superluminal components, because their knots could be separated into two groups (group-A and group-B) which need different patterns of precessing common trajectory to fit their kinematics, respectively.

It is worth noting the fact: Analysing the observational data in earlier years (i.e. the observational data on the knots of

group-A only), Klare (2005), Lobanov & Roland (2005) and Qian et al. (2009) suggested 3C345 having a precessing jet, while analysing the whole observational data on the knots of both group-A and group-B, Schinzel et al. (2011a) suggested no precession of the jet in 3C345. Thus the separation of the superluminal knots into two groups may be a plausible assumption for investigating the jet precession in 3C345, otherwise we would have to relinquish the assumption of jet precession for 3C345.

The full interpretation of the kinematics and flux evolution of the superluminal components in 3C345 demonstrates that our precessing nozzle scenario proposed for blazar 3C345 can interpret the kinematic, dynamic and emission properties of its superluminal components, although the assumption of a double jet structure is only a working hypothesis.

We have been trying to propose a scenario with a single precessing jet, as a significant alternative, to interpret the kinematics of the superluminal knots in 3C345 as a whole, because there seems a possibility that the knots of group-A and group-B can be combined into one group. For example, we may assume that the trajectory-pattern transition of the knots in the jet-B could occur at core distances  $r_n < 0.1$  mas and their innermost tracks could connect



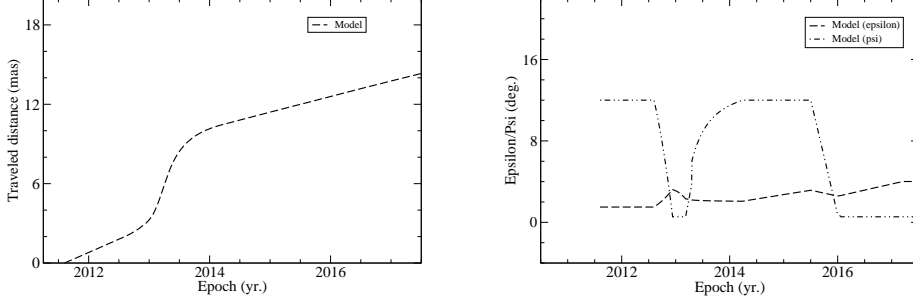


**Fig. 29.** Knot B7: the modeled traveled distance  $Z(t)$ , parameters  $\epsilon(t)$  and  $\psi(t)$  as functions of time. Before 2012.60  $\epsilon=1.50^\circ$  and  $\psi=12.0^\circ$ , knot B7 moved along the precessing common trajectory, while after 2012.60 both parameters started to change and knot B7 started to move along its own individual track, deviating from the precessing common track. Thus its transition from the precessing common trajectory to its individual track occurred at  $X_n=0.036$  mas, corresponding to a traveled distance  $Z=2.0$  mas=13.3 pc.

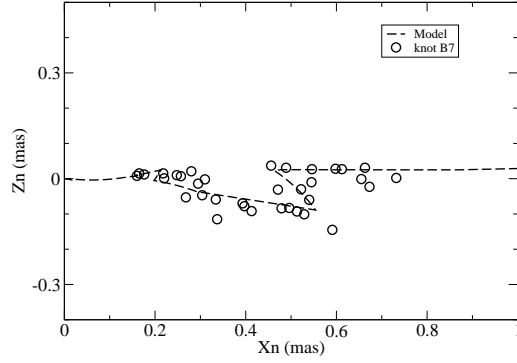


**Fig. 30.** Knot B7: Model fitting of the entire trajectory  $Z_n(X_n)$ . Within  $X_n=0.036$  mas knot B7 moved along the precessing common trajectory, while beyond  $X_n=0.036$  mas it started to move along its own individual trajectory. Thus only the individual track was observed and its precessing common track was not observed. The entire trajectory was very well fitted, especially the trajectory section of its backward motion near  $X_n\sim 0.5$  mas.

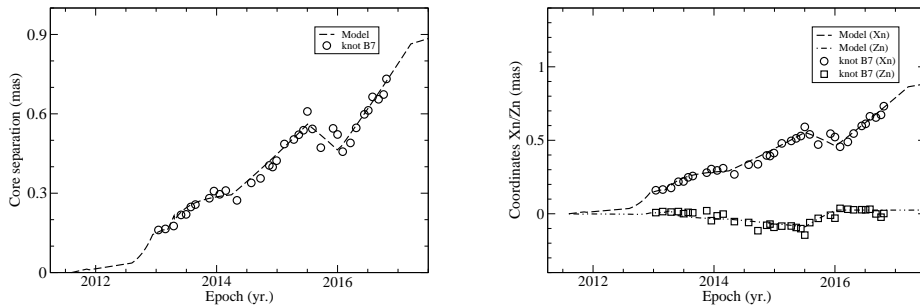


**Fig. 31.** Knot B7: Model fitting of the core separation  $r_n(t)$ , coordinates  $X_n(t)$  and  $Z_n(t)$ . They are all well fitted, especially for its backward motion near epoch 2016.

with the precessing common trajectory of jet-A at core distances  $r_n < 0.10\text{--}0.05$  mas. In such a scenario the observed tracks of the knots of group-B are only the outer trajectories beyond their trajectory-transitions, while their innermost tracks within the transitions ( $r_n \leq 0.05\text{--}0.1$  mas) have not been observed. The trajectory-transition observed in

the core-distance range of  $\sim 0.1\text{--}0.4$  mas in knot C8 (Qian 2022a) is an extremely instructive example. In this case the precession of the jet may be related to the precession of the disk around the black hole in the nucleus of 3C345. This kind of scenario with a single precessing jet nozzle should

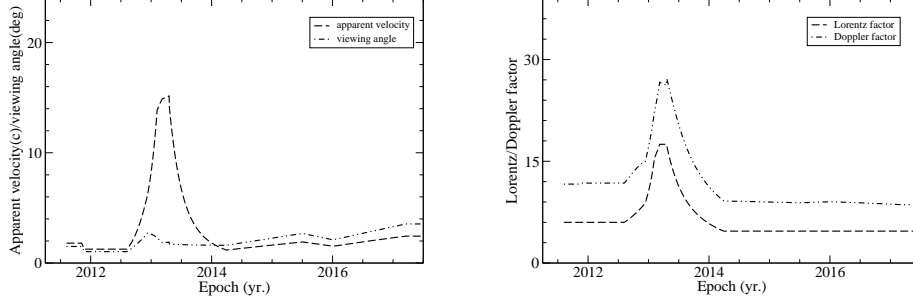


**Fig. 32.** Knot B7. Left panel: the model-derived apparent speed  $\beta_{app}(t)$  and viewing angle  $\theta(t)$  as functions of time. The apparent speed has a maximum  $\beta_{app,max}=15.15$  at 2013.30 and the corresponding viewing angle  $\theta=1.90^\circ$  and Lorentz factor  $\Gamma=17.50$ . Right panel: the model-derived bulk Lorentz factor  $\Gamma(t)$  and Doppler factor  $\delta(t)$  as continuous functions of time. The Doppler factor has a maximum  $\delta_{max}=27.16$  at 2013.30 and the corresponding Lorentz factor  $\Gamma=17.23$  and viewing angle  $\theta=1.72^\circ$ .

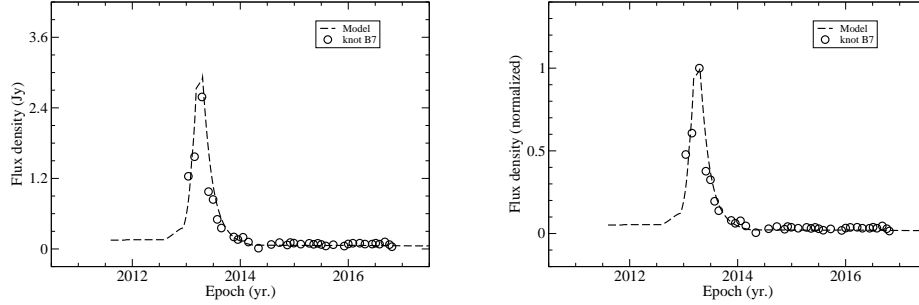


**Fig. 33.** Knot B7: Model fitting of the 43 GHz light curve (left panel) and its corresponding normalized light curve (right panel). They are well fitted by the model-derived Doppler boosting profile  $S_{int}[\delta(t)]^{3+\alpha}$  and  $[\delta(t)/\delta_{max}]^{3+\alpha}$ , respectively. An intrinsic flux density  $S_{int}=28.0\mu\text{Jy}$  and a spectral index  $\alpha=0.50$  are adopted.

be tested by the VLBI observations with higher resolutions in the future.

## References

- Babadzhanlyants M.K., Belokon E.T. & Gamm N.G., 1995, *Astronomy Report* 39, 393  
 Biretta J.A., Moore R.L. & Cohen M.H., 1986, *ApJ* 308, 93  
 Hardee P.E., 1987, *ApJ* 318, 78  
 Hogg D.W., 1999, *astro-ph/9905116*  
 Jorstad S.G., Marscher A.P., Lister M.L., et al., 2005, *AJ* 130, 1418  
 Klare J., 2003, *Quasi-Periodicity in the Parsec-Scale Jet of the Quasar 3C345*, PhD Thesis, Rheinische-Friedrich-Wilhelms-Universität Bonn, Bonn, Germany  
 Klare J., Zensus J.A., Lobanov A.P., et al., 2005, in "Future Directions in High resolution Astronomy: The 10th Anniversary of the VLBA", ASP Conference Series, Vol.340 (eds., J.D. Romney and M.J. Reid), p.40  
 Lobanov A.P. & Roland J., 2005, *A&A* 431, 831  
 Lobanov A.P. & Zensus J.A., 1999, *ApJ* 521, 509  
 Lobanov A.P. & Zensus J.A., 1994, in *Proc. Second EVN/JIVE Symposium*, ed. A.J. Kus, R.T. Schilizzi, K.M. Borkovski & L.I. Gurvits, 93  
 Malina R.F., et al., 1994, *AJ* 107, 751  
 Moore R.L. & Stockman H.S., 1984, *ApJ* 279, 465  
 Qian S.J., Witzel A., Krichbaum T.P., et al., 1991a, *Acta Astron. Sin.* 32, 369 (*Chin. Astro. Astrophys.* 16, 137 (1992))  
 Qian S.J., Krichbaum T.P., Witzel A., et al., 1991b, in: *High Energy Astrophysics: Compact Stars and Active Galaxies (Proceedings of the 3rd Chinese Academy of Sciences and Max-Planck Society*

- Workshop*, held 19-23, October 1990 in Huangshan, China, edited by Qibin Li, Singapore: World Scientific), p.80  
 Qian S.J., Krichbaum T.P., Zensus J.A., et al., 1996, *A&A* 308, 395  
 Qian S.J., Kudryavtva N.A., Britzen S., et al., 2007, *Chin. J. Astrophys.* 7, 364  
 Qian S.J., Witzel A., Zensus J.A., et al., 2009, *Research in Astron. Astrophys.* 9, 137  
 Qian S.J., 2011, *Research in Astron. Astrophys.* 11, 43  
 Qian S.J., 2012, *Research in Astron. Astrophys.* 12, 46  
 Qian S.J., 2013, *Research in Astron. Astrophys.* 13, 783  
 Qian S.J., Britzen S., Witzel A., et al., 2014, *Research in Astron. Astrophys.* 14, 249  
 Qian S.J., 2015, *Research in Astron. Astrophys.* 15, 687  
 Qian S.J., 2016, *Research in Astron. Astrophys.*, 16, 20  
 Qian S.J., Britzen S., Witzel A., et al., 2017, *A&A* 604, A90  
 Qian S.J., Britzen S., Witzel A., et al., 2018a, *A&A* 615, A123  
 Qian S.J., 2018b, *arXiv e-prints*, arXiv:1811.11514  
 Qian S.J., Britzen S., Krichbaum T.P., Witzel A., 2019, *A&A* 621, A11  
 Qian S.J., 2020, *arXiv e-prints*, arXiv:2005.05517  
 Qian S.J., Britzen S., Krichbaum T.P., Witzel A., 2021, *A&A* 653, A7  
 Qian S.J., 2022a, *arXiv e-prints*, arXiv:2202.01915  
 Qian S.J., 2022b, *arXiv e-prints*, arXiv:2206.14995  
 Qian S.J., 2023a, *arXiv e-prints*, arXiv:2306.05619  
 Qian S.J., 2023b, *arXiv e-prints*, arXiv:2306.06863  
 Ros E., Zensus J.A. & Lobanov A.P., 2000, *A&A* 354, 55  
 Schinzel F.K., 2011a, PhD thesis, University of Cologne  
 Schinzel F.K., Sokolovsky K.V., D'Ammando F., et al., 2011b, *A&A* 532, A150  
 Schinzel F.K., Lobanov A.P. & Zensus J.A., 2010a, in: *Accretion and Ejection in AGNs: A Global View*, ASP Conference Series,

- Vol.427 (2010), eds. L. Maraschi, G. Ghisellini, R. Della Ceca & F. Tavecchio
- Schinzel F.K., Lobanov A.P., Jorstad S.G., et al., 2010b: in "Fermi meets Jansky-AGN in Radio and Gamma Rays", eds. T. Savolainen, E. Ros, R.W. Porcas & J.A. Zensus
- Schramm R.-J., Borgeest U., Camenzind M., et al., 1993, A&A
- Spergel D.N., Verde L., Peilis H.V., et al., 2003, ApJS 148, 145
- Steffen W., Zensus J.A., Kirchbaum T.P., Witzel A., Qian S.J., 1995, A&A 302, 335
- Wang J.M., Luo B., Ho L.C., 2004, ApJ 615, L9
- Zensus J.A., 1997, ARA&A 35, 607
- Zensus J.A., Cohen M.H., Unwin S.C., 1995, ApJ 443, 35